Pharmacokinetic modeling of PSMA-targeted nanobubbles for quantification of extravasation and binding in mice models of prostate cancer

Please check the document version of this publication:

COMPREHENSIVE MACHINE QA SOLUTIONS
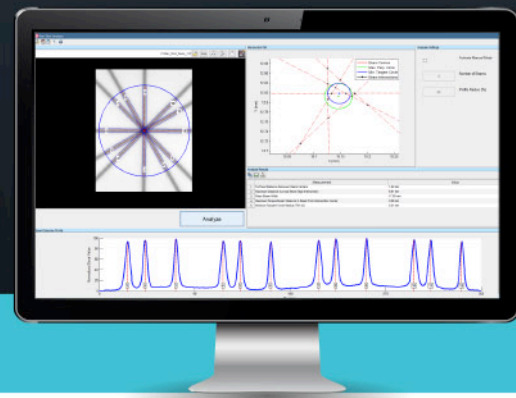
FROM RADIOLOGICAL IMAGING TECHNOLOGY, INC.

RIT provides extensive machine QA capabilities, including comprehensive software packages that can be used to perform a full suite of measurements in accordance with TG-142, TG-148, and/or TG-135. RIT's automated routines allow you to perform daily, monthly, and annual QA with efficiency and precision, all while giving you confidence knowing your delivery performance is optimized.

TG-142: LINEAR ACCELERATORS

RIT is the single-vendor software solution that performs and trends every test recommended in TG-142.

Perform comprehensive quality assurance of Varian, Elekta, and all linear accelerators with confidence and ease, using your EPID and RIT software. Several packages feature RIT's popular 3D Winston-Lutz Isocenter Optimization routine that will help your SRS/SBRT delivery with its sub-millimeter, fully-automated accuracy. RIT offers automated tests for Star Shot Analysis, Radiation vs. Light Field, MLC accuracy, and many others.

RITG142

TG-148: HELICAL TOMOTHERAPY®

RITG148+
Radixact

RIT offers a comprehensive test suite for helical TomoTherapy® and Radixact® machines, in accordance with TG-148.

Designed with the TG-148 report in mind, the RITG148+ and RIT *Complete* software packages analyze the standardized tests for helical TomoTherapy machine QA. These include Static & Rotational Output Consistency, Jaw Centering and Alignment, Overhead Laser Positioning, Interrupted Treatment, and all others recommended for daily, monthly, and annual QA. The software will also analyze image quality using the TomoTherapy Cheese phantom.

TG-135: CYBERKNIFE® ROBOTIC RADIOSURGERY

RIT provides a comprehensive test suite for CyberKnife® and all robotic radiosurgery, in accordance with TG-135.

The RITG135 and RIT *Complete* software packages contain five fully-automated QA tests for CyberKnife® machines: End-to-End Test, AQA Test, Iris Test, Laser Coincidence, and MLC (Garden Fence) Test for the M6 Collimator. Combining a user-friendly interface with automated film detection algorithms, the software eliminates the need for manual manipulation or alignment of images, and drastically reduces the time required to perform these tests.

RITG135

TomoTherapy®, Radixact®, and CyberKnife® are registered trademarks of Accuray, Inc.

RIT®

VISIT **RADIMAGE.COM** TO DEMO RIT'S ADVANCED RANGE OF MACHINE QA, MLC QA, PATIENT QA, AND IMAGING QA ROUTINES.

📞 **+1 (719) 590-1077, OPT. 4**

✉ **SALES@RADIMAGE.COM**

Connect with us on social media

@RIT4QA 🅕 🅣 in

RESEARCH ARTICLE

Pharmacokinetic modeling of PSMA-targeted nanobubbles for quantification of extravasation and binding in mice models of prostate cancer

Chuan Chen[1] | Reshani Perera[2] | Michael C. Kolios[3] | Hessel Wijkstra[1] | Massimo Mischi[1] | Agata A. Exner[2] | Simona Turco[1]

[1]Electrical Engineering Department, Eindhoven University of Technology, Eindhoven, The Netherlands

[2]Department of Radiology, Case Western Reserve University, Cleveland, Ohio, USA

[3]Department of Physics, Toronto Metropolitan University, Toronto, Ontario, Canada

Correspondence
Chuan Chen, Eindhoven University of Technology, Eindhoven, The Netherlands.
Email: C.Chen3@tue.nl

Abstract

Purpose: Contrast-enhanced ultrasound (CEUS) by injection of microbubbles (MBs) has shown promise as a cost-effective imaging modality for prostate cancer (PCa) detection. More recently, nanobubbles (NBs) have been proposed as novel ultrasound contrast agents. Unlike MBs, which are intravascular ultrasound contrast agents, the smaller diameter of NBs allows them to cross the vessel wall and target specific receptors on cancer cells such as the prostate-specific membrane antigen (PSMA). It has been demonstrated that PSMA-targeted NBs can bind to the receptors of PCa cells and show a prolonged retention effect in dual-tumor mice models. However, the analysis of the prolonged retention effect has so far been limited to qualitative or semi-quantitative approaches.

Methods: This work introduces two pharmacokinetics models for quantitative analysis of time–intensity curves (TICs) obtained from the CEUS loops. The first model is based on describing the vascular input by the modified local density random walk (mLDRW) model and independently interprets TICs from each tumor lesion. Differently, the second model is based on the reference-tissue model, previously proposed in the context of nuclear imaging, and describes the binding kinetics of an indicator in a target tissue by using a reference tissue where binding does not occur.

Results: Our results show that four estimated parameters, $\beta, \beta/\lambda, \beta_+/\beta_-$, for the mLDRW-input model, and γ for the reference-based model, were significantly different (p-value <0.05) between free NBs and PSMA-NBs. These parameters estimated by the two models demonstrate different behaviors between PSMA-targeted and free NBs.

Conclusions: These promising results encourage further quantitative analysis of targeted NBs for improved cancer diagnostics and characterization.

KEYWORDS
contrast-enhanced ultrasound, molecular imaging, nanobubbles, pharmacokinetic modeling, prostate cancer

1 | INTRODUCTION

Prostate cancer (PCa) is the most prevalent type of cancer and the second leading cause of cancer death in males of Western countries.[1–3] Although several efforts have been devoted, efficient detection and diagnosis of PCa remain challenging in clinical practice.[4] The suspicion of PCa is usually diagnosed by elevated serum prostate-specific antigen (PSA) or suspicious digital rectal examination (DRE).[5,6] The suspicious PCa lesions are further detected by systematic biopsies that obtain a number of glandular materials

samples for histologic examinations. Apart from the high cost and risk of infection, systematic biopsies may lead to either undertreatment or overtreatment of the disease.[7] Recently, multiparametric magnetic resonance imaging (MRI) has gained attention for noninvasive diagnosis of PCa.[8] However, its application in clinical routine is still hampered by the limited accessibility of the equipment, possibility of missing clinically significant PCa, and difficulty of interpreting the results.[9]

More recently, transrectal ultrasonography (TRUS) also shows promise as a cost-effective alternative for improving the detection and localization of PCa.[10,11] In particular, contrast-enhanced ultrasound (CEUS) is a promising modality for improving the detection of PCa by imaging cancer angiogenesis.[12,13] Typical ultrasound contrast agents (UCA) consist of microbubbles (MBs) with a diameter of 1–10 μm. MBs permit visualization and assessment of the microvasculature when injected into the bloodstream and sensed by dedicated contrast-specific ultrasound scanning sequences. Due to cancer angiogenesis, the microvasculature is typically altered in PCa, exhibiting high microvascular density, along with increased extravascular leakage and vascular tortuosity.[14] Dedicated methods have been developed to detect PCa by angiogenesis imaging based on MBs CEUS acquisitions.[15,16] Moreover, molecular ultrasound imaging by MBs targeted to the vascular endothelial growth factor receptor 2 has also been explored for the detection of PCa. However, a limited PCa detection rate of 65% was achieved in a phase-0 clinical trial based on qualitative analysis.[17]

Although being an optimal intravascular contrast agent for vascular assessment, their relatively large diameter keeps targeted MBs from crossing the vascular endothelium and reaching molecules expressed on the tumor cell surface. This restriction can be overcome by new-generation UCAs, nanobubbles (NBs), whose diameter is about 10 times smaller compared to MBs, hence facilitating them to cross the vessel wall.[18–20] Through the nonlinear interaction with echo pulses, the intra- and extra-vascular pharmacokinetics of NBs can be visualized with adequate ultrasound contrast enhancement during their extended circulation span.[21–23] Furthermore, NBs can target specific molecules, such as prostate-specific membrane antigen (PSMA), to actively bind to the receptors overexpressed in PCa cells.[24,25] As shown by nuclear imaging, PSMA is an important biomarker that is overexpressed in PCa.[26] The specific binding of PSMA-targeted NBs (PSMA-NB) on tumor cells expressing PSMA was demonstrated both in vivo, by a prolonged retention time in mice models of PCa, and ex vivo, by follow-up histological examination.[27,28]

In relevant studies, the prolonged retention effect owning to NB extravasation or specific binding was analyzed by interpreting average UCA time–intensity curves (TICs) within a region of interest (ROI).[23,27] However, the analysis was primarily qualitative or semi-quantitative, without quantitative assessment of the PSMA-NB pharmacokinetics. Pharmacokinetic models of contrast agent intravascular flow, extravasation, and specific binding have previously been studied in MB-based CEUS, dynamic contrast-enhanced (DCE) MRI, and nuclear imaging[29–32]; these studies provide a valuable reference to model the behavior of NBs in CEUS. The main approach investigated in previous studies was based on compartmental modeling, which is widely used to describe transport phenomena in biological systems.[33,34] The compartmental modeling usually requires an approximation or measurement of the vascular input for the system. This work introduces two pharmacokinetic models to quantitatively analyze the extravasation and binding effects of PSMA-NBs in a mouse model consisting of dual tumors—one expressing PSMA and one control tumor, which is PSMA-negative. The first pharmacokinetic model employs a modified local density random walk (mLDRW) model as the vascular input to separately interpret the TIC from each tumor.[32,35] Although this model has the advantage of independently analyzing a single TIC, it requires the assumption that the mLDRW model well describes the vascular input function; moreover, a larger number of fitting parameters is necessary. On the other hand, the reference-tissue model utilizes the TIC from one tumor as a reference to depict the TIC from the other tumor,[30] and it is thus particularly suitable for the dual-tumor animal model. However, its applicability is limited to cases where a reference tissue is present in the field of view; moreover, independent pixel fitting is hampered. The models were applied to seven dual-tumor mouse models of PCa.[27] For each mouse, TICs obtained from the CEUS loops were fitted by these models to extract quantitative parameters related to NBs extravasation, retention, and binding. Pharmacokinetic modeling of contrast agent intravascular flow, extravasation, and specific binding has been studied separately in MB-based CEUS, DCE-MRI, and nuclear imaging, respectively[29–32]; however, to the best of our knowledge, previous pharmacokinetic studies have never addressed extravasation of NB as the UCA. Thus, we adapted previous methods to be able to describe and interpret the behavior of PSMA-NBs in a dual-tumor mouse model. Several parameters from both models suggested significant differences between free and PSMA-NBs. These parameters quantified the prolonged retention effect caused by the specific binding of PSMA-NBs. The proposed models have the potential to improve the detection of PCa by enabling more accurate transrectal ultrasound-guided biopsies, and thus reducing the need for systematic biopsies.

2 | METHODS AND MATERIALS

2.1 | Preparation of NBs and PSMA-NBs

Nanobubbles were formulated as previously described.[27] Briefly, a lipid solution in propylene glycol (10 mg/ml) was prepared using 1,2-dibehenoyl-sn-glycero-3-phosphocholine (DBPC, Avanti Polar Lipids Inc., Pelham, AL), 1,2-dipalmitoyl-sn-glycero-3-phosphate (DPPA), 1,2-dipalmitoyl-sn-glycero-3-phosphor ethanolamine (DPPE, Corden Pharma, Switzerland), and 1,2-distearoyl-sn-glycero-3-phosphoethanolamine-N-[methoxy (polyethylene glycol)-2000] (ammonium salt) (DSPE-mPEG 2000, Laysan Lipids, Arab, AL) with a 6:1:2:1 ratio by heating and sonicating at $80°C$. A solution of glycerol (Gly, Acros Organics) in phosphate buffer saline (0.15 g/ml, pH 7.4) was added to the lipids and sonicated for 10 min at room temperature. The solution (1 ml) was transferred to a 3-ml vial, capped with a rubber septum and aluminum seal. Air was replaced by octafluoropropane (C3F8, Electronic Fluorocarbons, LLC, PA) gas and nanobubbles formed by mechanical shaking with a VialMix shaker (Bristol-Myers Squibb Medical Imaging Inc., N. Billerica, MA) for 45 s. Nanobubbles were isolated from the microbubbles by centrifugation at 50 rcf for 5 min with the headspace vial inverted, and the 100 μl NB solution withdrawn from a fixed distance of 5 mm from the bottom with a 21 G needle.

PSMA-NBs were prepared by adding DSPE-PEG-PSMA-1 (25 μg/ml) to the initial lipid solution and following the above protocol. To prepare DSPE-PEG-PSMA-1, PSMA-1 (from Prof. James Basilion lab) was mixed with DSPE-PEG-MAL (1,2-distearoyl-sn-glycero-3-phospho ethanolamine-N-methoxy(polyethylene glycol)-2000-Maleimide, Laysan Bio, Arab, AL) in 1:2 ratio at pH 8.0 in PBS. After combining, the mixture was vortexed thoroughly and was reacted for 4 h on the vial rotator at $4°C$. The product was lyophilized, and the resultant powder was dissolved in PBS to obtain DSPE-PEG-PSMA-1 stock solution. Based on our experiment,[27] we approximated that the total amount of PSMA on a bubble was 35×10^3 molecules. We also carried out standard fluorescence microscope imaging and confocal imaging to provide evidence that PSMA-expressing PC3pip cells selectively uptake PSMA-NB compared to the free NB (see Figure 1a,b).[36] The red fluorescence of NB and PSMA-NB comes from rhodamine. The nanobubble diameter and the concentration were characterized by using resonant mass measurement (RMM).[27] The RMM experiment shows that the diameter of NB and PSMA-NB was 281 ± 2 and 277 ± 11 nm, respectively. The concentration of NB and PSMA-NB was $3.9 \times 10^{11} \pm 2.82 \times 10^{10}$ and $4 \times 10^{11} \pm 2.45 \times 10^{10}$ NB/ml. The size distribution and the concentration of NBs and PSMA-NBs are presented in Figure 1c.

2.2 | Animal models and CEUS imaging

Animals were handled according to a protocol approved by the Institutional Animal Care and Use Committee (IACUC, #2016-0024) at Case Western Reserve University and were in accordance with all applicable protocols and guidelines in regards to animal use. Seven male athymic nude mice between 4 and 6 weeks old were included for acquiring CEUS images. These mice were anesthetized by inhalation of 3% isoflurane with 1 L/min oxygen. A dual-tumor model was initiated by subcutaneously injecting 1×10^6 PSMA-negative PC3flu and PSMA-positive PC3pip cells in 100 μl matrigel. Animals were observed every other day until tumors' diameter reached 8–10 mm.

Before acquiring CEUS images, 200-μl free NBs or PSMA-NBs over 30–40 s were administrated via the tail vein using a 26 G catheter. We selected 200 μl for the injection as the optimal volume with high contrast enhancement and no adverse effect. For CEUS imaging, a PLT-1204BT probe (central frequency: 12 MHz; MI: 0.1; dynamic range: 65 dB; gain: 70 dB; imaging frame rate: 0.2 frames/s) was fixated to visualize both PC3flu and PC3pip tumors in the same field of view. The experimental setup is as illustrated in Figure 2a. After 30 min of CEUS imaging, high-intensity flashes were employed to destruct the remaining NBs. Thirty minutes later (1 h after the first injection), the same mouse received 200-μl of the other UCA type (either PSMA-NBs or free NBs). Apart from free NBs and PSMA-NBs, Lumason MBs (sulfur hexafluoride lipid-type A microspheres, Bracco Diagnostics Inc.) were also administrated for acquiring conventional CEUS 30 min after the NB-CEUS (1 h after first injection, the contrast reached the baseline level), as a reference to be compared with the NB-CEUS. After the CEUS acquisition, mice were euthanized 24 h post injection for the histological analysis.

As shown in Figure 2b, on the acquired CEUS images of PSMA-NB, we manually delineated two ROIs for positioning both PC3flu (notated as PSMA-negative ROI) and PC3pip (notated as PSMA-positive ROI) tumors. From each ROI, one TIC was extracted by recording the evolution of the average dB-scaled contrast enhancement over time. In Figure 2c, one example of TIC extraction from the PSMA-negative ROI (the blue region on the left side) and from the PSMA-positive ROI (the red region on the right side) is shown. The dB-scaled TIC was then linearized into absolute acoustic intensity,[29] the TIC was resampled at 1 Hz frequency, and finally the TIC was filtered by a low-pass filter with a passband frequency of 0.02 Hz for further quantitative analyses.

Afterward, we examined the PSMA expression in tumor tissues by using immunohistochemistry analysis. First, tumor tissues were cut into 10 μm slices and washed three times with phosphate buffer saline (PBS). The tissue slices were incubated in protein blocking solution that contains 0.5% TritonX-100, and then
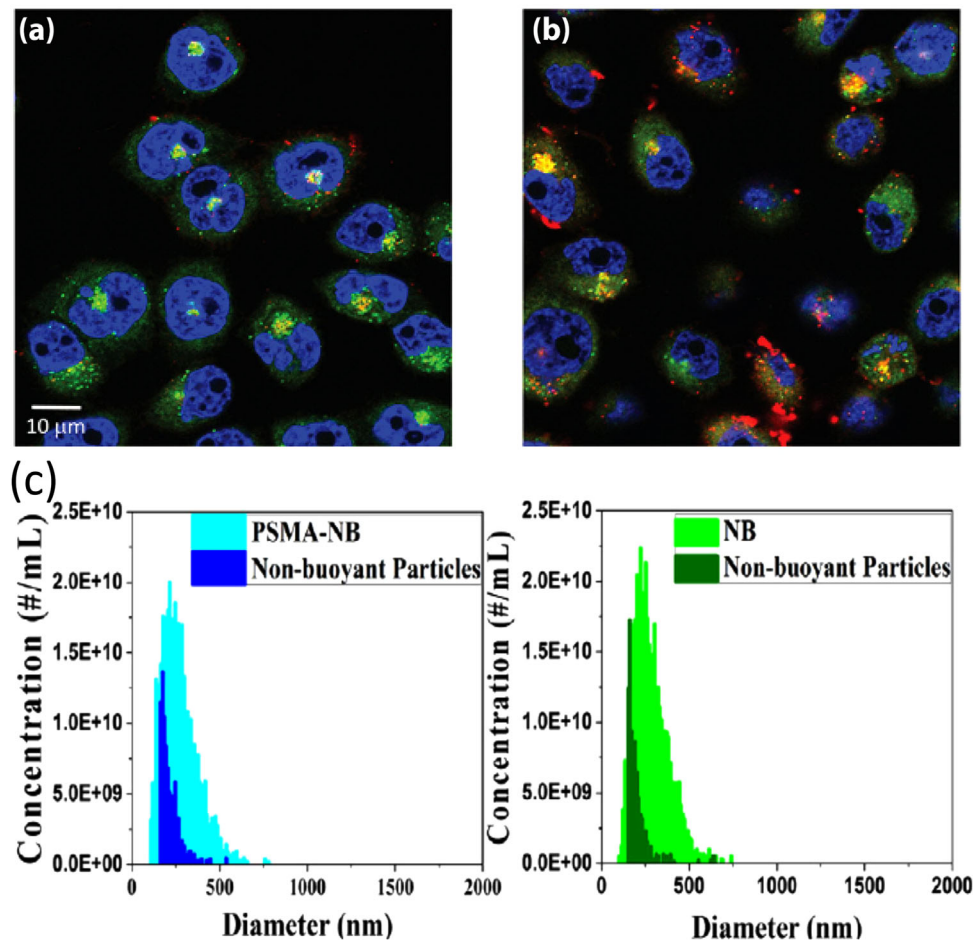
FIGURE 1 Representative confocal images of (a) NB and (b) PSMA-NB distribution in PC3pip cells. 100× (blue-nuclei, red-NB, and green-late endosome/lysosomes), yellow-co-localized bubbles in late endosome/lysosomes. PSMA-NB shows high co-localization in late endosomal/lysosomal vesicles (yellow). (c) Size distribution and the concentration of NBs and PSMA-NBs acquired via resonant mass measurement. Nonbuoyant particles refer to liposomes, micelles, lipid debris, and so forth.

incubated in 1:150 diluted PSMA primary antibody for 24 h at 4°C. After being washed with PBS, the tissue was incubated with Alexa-568-tagged secondary antibody for 1 h, and it was stained with DAPI. We obtained the fluorescence images and quantified the overexpression of PSMA in PC3pip tumor tissues in both rim and core areas (see Figure 3).

2.3 | Pharmacokinetic models

As free NBs or PSMA-NBs flow through the vascular circulation, a fraction of them extravasates to enter the interstitial space. PSMA-NBs can further bind to PCa cells that overexpress PSMA. The extravasation and specific binding are manifested as a prolonged retention effect in the TIC. The derivations of the following two models are described in the Supporting Materials. To interpret the prolonged retention effect, we introduced two pharmacokinetic models for fitting

the TIC. The first model employs the mLDRW[15,37] as the plasma input. The other model is based on the simplified reference-based tissue model[30] and utilizes the TIC from the PSMA-negative ROI as a reference input function to depict the TIC in the PSMA-positive tumor ROI.[35] The first model that employs the mLDRW is termed as mLDRW-input model from here on. The second model that utilizes a reference ROI is termed as the reference-based model from here on.

For the mLDRW-input model, both TIC ($I_+(t)$) from PSMA-positive and TIC ($I_-(t)$) PSMA-negative ROIs were fitted by the following model with an input function I_p:

$$I_\pm(t) = I_p(t) + \beta I_p(t) * e^{-\lambda t}, \tag{1}$$

where β represents the residual factor of remaining enhancement after washing out the input, * is the convolution operator, and λ is the decay rate.
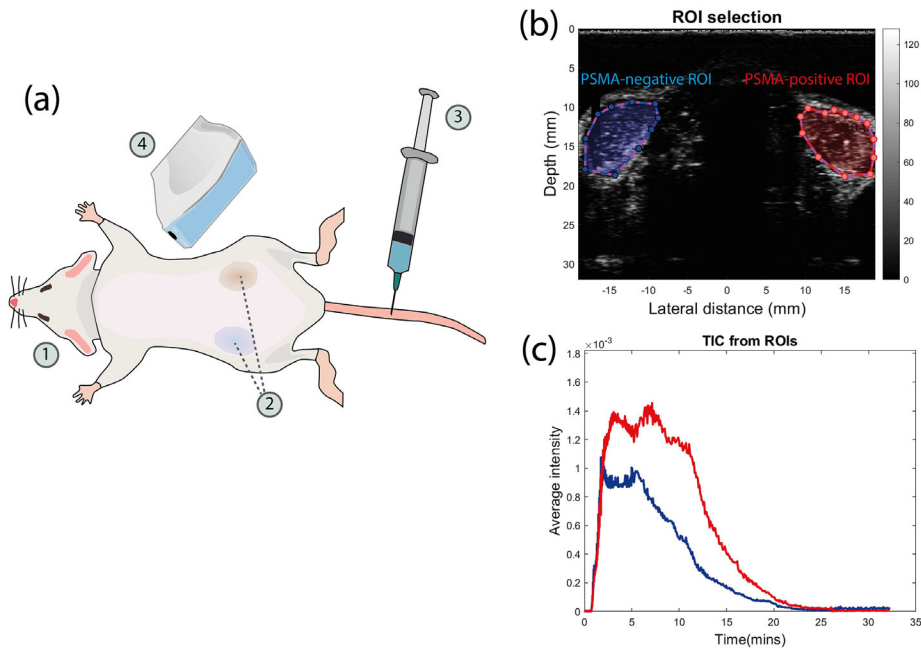
FIGURE 2 Illustration of the experimental setup and example of ROI-based TIC. (a) The workflow includes four parts: (1) anesthetized male athymic nude mouse, (2) subcutaneously implanted dual-tumor, (3) administration of 200-μl bolus of either free NBs or PSMA-NBs via the tail vein, and (4) Imaging using an ultrasound probe. (b) Example of manually delineated PSMA-negative ROI (the blue region on the left side) and PSMA-positive ROI (the red region on the right side) on the CEUS of PSMA-NB. The colorbar represents the gray level of CEUS image ranging from 0 to 128. (c) Average TIC (blue) from the PSMA-negative ROI and average TIC (red) from the PSMA-positive ROI
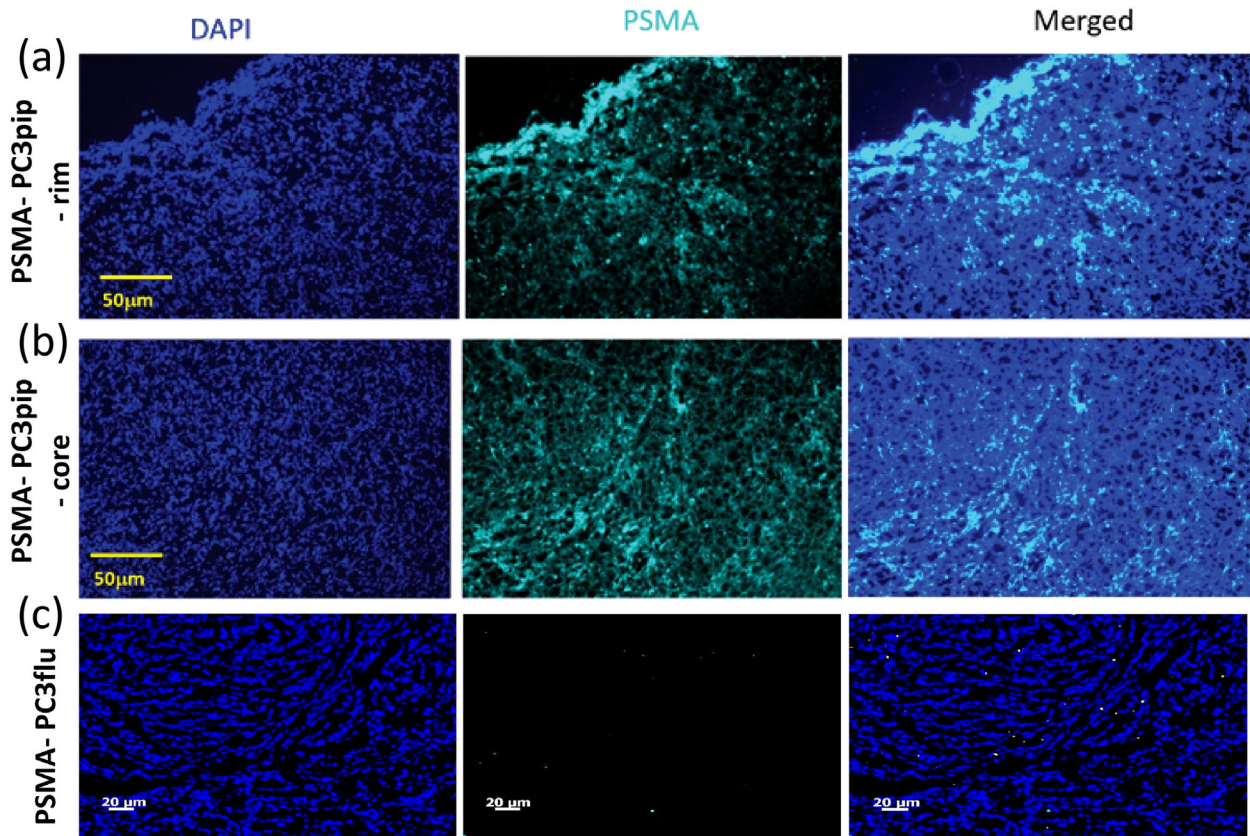
FIGURE 3 Representative fluorescence images of (a) PSMA expression in the rim of PC3pip tumor, (b) PSMA expression in the core of PC3pip tumor, and (c) PSMA expression in PC3flu tumor. The blue color is the nuclei. The cyan color represents PSMA expression. The PSMA expression disseminated uniformly in both tumor rim and tumor core in PC3pip tumor tissues (66.49 ± 5.44 vs. $59.09 \pm 6.75, p = 0.06$).

The input function $I_p(t)$ is modeled by the mLDRW as

$$I_p(t) = \alpha \sqrt{\frac{\kappa}{2\pi(t - t_0)}} e^{-\frac{\kappa(t - t_0 - \mu)^2}{2(t - t_0)}}. \qquad (2)$$

where α represents the area under the curve of $I_p(t)$, μ is the mean transit time, t_0 is the theoretical injection time, and κ represents the skewness parameter given by the local ratio between the squared velocity and the dispersion parameter.

To improve the efficiency of curve-fitting algorithm, we transformed the theoretical expression of the mLDRW-input model, involving a convolution, into a closed-form solution based on the derivation in Turco et al.[29]

For the reference-based model, TIC ($I_+(t)$) was regarded from the PSMA-positive ROI as a function of the input TIC ($I_-(t)$) from the PSMA-negative ROI. As derived in Lammertsma and Hume,[30] a simplified relationship was used as

$$I_+(t) = R_r I_-(t) + \left(k_2 - R_r \frac{k_2}{1 + \gamma}\right) I_-(t) * e^{-\frac{k_2}{1+\gamma}t}. \qquad (3)$$

Here, $R_r = k_1/k'_1$ accounts for the ratio of delivering NBs to the PSMA-positive ROI and PSMA-negative ROI, γ is regarded as the approximate binding potential due to specific binding. In the derivation of the above model, there is one underlying assumption that the distribution volume of tissue and vascularity is the same for the two tumor ROIs to allow $k_1/k_2 = k'_1/k'_2$. This assumption yields valid for our experiments, because two tumors were initiated at comparable positions to grow as lesions with comparable characteristics. We have not observed an apparent difference in their tumor appearance on B-mode and overall enhancement levels on CEUS for all mice. A more detailed derivation of this simplified model is presented in (A.13) to (A.15) of the Supporting Materials. In this derivation, one can notice the role of γ in relating the equivalent transfer rate k_{2a} and actual transfer rate k_2 as $k_{2a} = k_2/(1 + \gamma)$. In the literature,[26] γ was strictly defined as a positive-value parameter, because the specific binding was assumed to always produce a longer retention time in the target ROI than the reference ROI free of specific binding. Whereas for the free NBs, the relative difference of retention effect between the PSMA-negative and PSMA-positive tumor ROIs is unlikely to be caused by the specific binding effect. Therefore, we allow γ to take a negative value to account for the possibility that the retention effect is greater in the PSMA-negative ROI than the PSMA-positive ROI.

2.4 | Numerical curve fitting method

The above two models were fitted to the experimental TICs extracted from the PSMA-positive ROI and PSMA-negative ROI through numerical computation. With regards to the mLDRW-input model, the fitting process was performed by least-square fitting with the trust-region reflective algorithm, as implemented in MATLAB platform (MATLAB R2020a). We approximated the initial values, as well as the upper and lower bounds for each parameter, based on the measured time to peak (TTP), peak enhancement (PE), area under the curve (AUC), and wash-out rate (WoR). For the parameter t_0, we implemented an iterative grid search, which spanned from 45 to 75 s in 1-s steps. Finally, we chose the optimal parameters by the minimum mean-square error criterion.

With regards to the reference-based model, the estimation was performed by a grid search. To speed up the computation, the search was bounded within specific ranges for each parameter. Similar to,[27] we adopted the basis function method to increase robustness and decrease the computation time of curve fitting. By the basis-function approach, the model was represented by a set of basis function in the following form:

$$I_+(t) = \theta_1 I_-(t) + \theta_1 \theta_2 I_-(t) * e^{-\theta_3 t}, \qquad (4)$$

where $\theta_1 = R_r, \theta_2 = k_2 \left(\frac{1}{R_r} - \frac{1}{1+\gamma}\right)$, and $\theta_3 = \frac{k_2}{1+\gamma}$.

Before the grid search, we calculated the ratio between I_+ and I_- PE as A_r. The grid for θ_1 was equally divided in the range $[0.02, 4] \times A_r$ into 200 steps. The selection of this range is based on the observation that the relative ratio of the maximum values of I_- and I_+ is restrained within $[1/4, 4]$. After a coarse-to-fine searching, the grid for θ_3 is refined in the range $[0.5, 50]$ with 100 equal steps in between. The grid for θ_3 was equally divide in the range $[0.5, 50]$ into 100 steps. For a given θ_3 value, the optimal θ_2 was searched within the range $[-1, 2] \times \theta_3$ by 151 steps. The reason for multiplying with θ_3 is to regard the division by the AUC of $e^{-\theta_3 t}$ ($t > 0$) that equals $1/\theta_3$. It is worthwhile to mention that the scaling factor θ_2 in the original literature was replaced by the product $\theta_1 \theta_2$ for highlighting the relative contribution of the convolution relation $I_-(t) * e^{-\theta_3 t}$ to the overall AUC. This modification can aid us to reduce the range of the grid search after normalization by the θ_1 value.

The quality of curve fitting was quantitatively evaluated by the normalized error R, which represents the ratio of mean square error to the experimental TIC norm as

$$R = \frac{\|I_t(t) - I_e(t)\|}{\|I_e(t)\|}, \qquad (5)$$

where $I_e(t)$, $I_t(t)$, and $\|\cdot\|$ represent the experimental TIC, the theoretical TIC, and the Euclidean norm, respectively. We evaluated the two models by comparing the estimated parameters in the PSMA-positive and PSMA-negative tumors after injection of free NBs and

TABLE 1   Estimated parameters by the mLDRW-input model

	Free NBs				PSMA-NBs				MBs			
	κ	β	λ	R	κ	β	λ	R	κ	β	λ	R
	PSMA− PSMA+	PSMA− PSMA+	PSMA− PSMA+	PSMA− PSMA+	PSMA− PSMA+	PSMA− PSMA+	PSMA− PSMA+	PSMA− PSMA+	PSMA− PSMA+	PSMA− PSMA+	PSMA− PSMA+	PSMA− PSMA+
Mouse 1	4.06	4.64	0.168	0.09	0.16	1.66	0.083	0.08	7.07	0.11	0.369	0.04
	4.12	1.53	0.243	0.08	0.18	2.66	0.091	0.10	5.56	0.04	0.213	0.02
Mouse 2	4.52	1.69	0.152	0.09	0.44	3.59	0.221	0.05	4.93	0.03	0.138	0.08
	4.68	1.43	0.136	0.15	0.55	4.51	0.273	0.08	5.01	0.05	0.020	0.17
Mouse 3	3.83	1.31	0.436	0.11	0.66	0.82	0.332	0.09	4.67	0.04	0.524	0.06
	5.63	0.91	0.392	0.25	0.73	2.76	0.365	0.12	8.93	0.13	0.058	0.08
Mouse 4	0.88	2.75	0.439	0.10	0.54	2.57	0.269	0.11	9.59	0.08	0.831	0.07
	1.01	1.54	0.161	0.08	3.06	3.26	0.087	0.11	8.95	0.19	0.856	0.07
Mouse 5	0.50	6.45	0.248	0.26	0.67	3.23	0.337	0.12	14.93	0.02	0.636	0.05
	0.94	3.20	0.470	0.26	0.85	8.65	0.110	0.24	15.15	0.03	0.514	0.04
Mouse 6	1.68	0.10	0.507	0.06	2.46	0.78	0.481	0.10	6.34	0.04	0.187	0.10
	1.05	0.12	0.385	0.06	2.60	0.24	0.308	0.10	10.2	0.08	0.128	0.10
Mouse 7	3.07	0.85	0.193	0.11	2.14	1.64	0.154	0.05	2.27	0.01	0.020	0.10
	5.81	0.68	0.194	0.07	3.39	2.57	0.167	0.08	1.27	0.04	0.480	0.10

Note: The estimated skewness parameter κ, residual factor β, and decaying rate λ are listed for seven mice, with free NBs, PSMA-NBs, and MBs presented in three major columns. For each parameter, the estimated values from the PSMA-negative (PSMA−) and PSMA-positive (PSMA+) ROIs are listed in the upper and bottom rows, respectively.

Abbreviations: NB, nanobubble; PSMA, prostate-specific membrane antigen; PSMA-NB, PSMA-targeted NB.

PSMA-NBs. The statistical significance (*p*-value) of the differences in the estimated parameters was assessed by the Kolmogorov–Smirnov test.

3 | RESULTS

The estimated skewness parameter κ, residual factor β, and decay rate λ, and the normalized error R by the mLDRW-input model are listed in Table 1. With regards to each mouse, R was overall higher in PSMA-positive ROIs than PSMA-negative ROIs using PSMA-NBs. The difference was not statistically significant between different groups due to the large variation of R across mice. Compared to free NBs or PSMA-NBs, the β value for MBs is significantly lower (*p*-value <0.01) to have a majority $\beta < 0.1$. To aid in comparing the estimated parameters, different values of κ, β, and λ between PSMA-negative ROIs and PSMA-positive ROIs, using free or PSMA-NBs are displayed in Figure 4a–c. For β, it was observed that β in PSMA-positive ROIs is mostly higher than the value in PSMA-negative ROIs, with the only exception of mouse 6, when using PSMA-NBs. This difference was not observed for free NBs. The ratio of β and λ is also displayed in Figure 4d for additional comparison. Figure 5 shows three examples of fitting the mLDRW-input model to the experimental TICs obtained in mice 1, 5, and 6. In the example of mouse 1, the mLDRW-input model produced high accuracy in fitting

the TICs of free NBs and relatively lower accuracy in fitting the TICs of PSMA-NBs. The example of mouse 5 shows a relatively less accurate curve fitting for both free and PSMA-NBs. It can also be noted that mouse 6 shows shorter prolonged retention in the PSMA-positive ROI when using the PSMA-NBs, which might explain the unexpected β values for this mouse.

For the reference-based model, the estimated parameter values for the input delivering ratio R_r, rate constant k_2, binding potential γ, and the normalized error R are listed in Table 2. In this table, one noticeable difference is that the estimated γ values are positive for PSMA-NBs and negative for free NBs. With regards to k_2, a similar trend as β from the mLDRW-input model was observed: The k_2 values for PSMA-NBs are mostly higher than the values for free NBs, except for mouse 6. In Figure 4f,g, the estimated k_2 and γ are compared between PSMA-NBs and free NBs.

Unlike Figure 4a–d, the plots in Figure 4f,g consist of only two groups of samples because the reference-based model combines the TICs from both PSMA-negative and PSMA-positive ROIs. To better compare the two methods, we additionally investigated the ratio between β_+ (β from the PSMA-positive ROI) and β_- (β from the PSMA-negative ROI), obtained from the mLDRW-input model; the results are shown in Figure 4e. For the reference-based model, three examples of curve fitting are displayed in Figure 6. It can be observed from both examples that the reference-based model
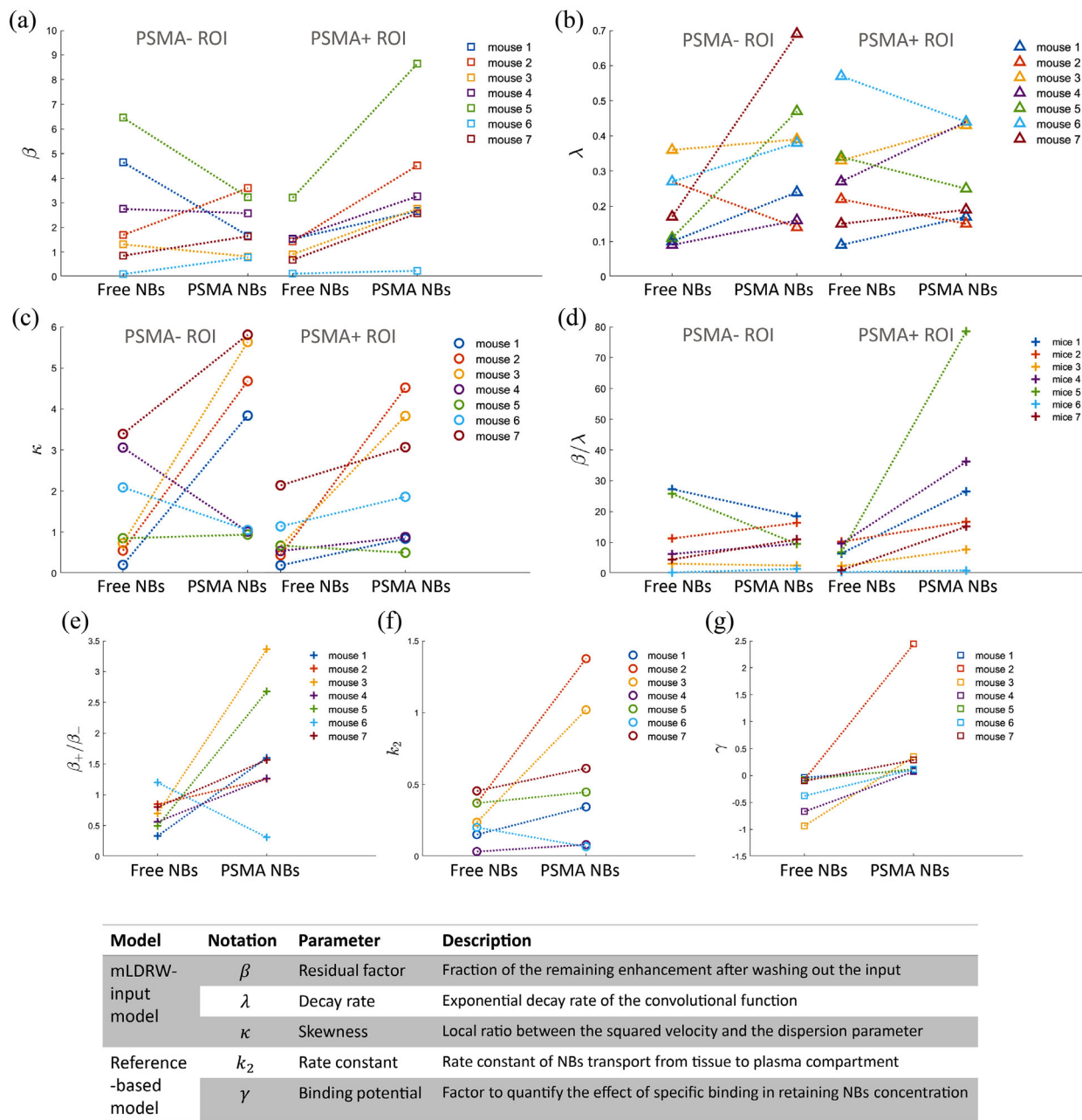
FIGURE 4 Plots of the estimated parameters by the two models. (a–d) The estimated residual factor β, decay rate λ, skewness parameter κ, and the ratio β/λ from the mLDRW-input model are presented. In each subfigure, the parameter values for free NBs and PSMA-NBs are compared by connected dashed lines for seven mice, with the PSMA-negative ROI (PSMA−) on the left side and PSMA-positive ROI (PSMA+) on the right side. (e–g) The estimated ratio of β_+ from PSMA-positive ROI and β_- from PSMA-negative ROI, the estimated rate constant k_2, and the binding potential γ from the reference-based model are compared by connected dashed lines between the free NBs and PSMA-NBs. The interpretation of these parameters is briefly described in the tables. ROI = region of interest; TIC = time-intensity curve; NB = nanobubble; PSMA = prostate-specific membrane antigen; PSMA-NB = PSMA-targeted NB; mLDRW = modified local density random walk

produced worse curve fitting in comparison with the mLDRW-input model. This comparison was also quantitatively evaluated by the normalized error R whose value was overall higher in the reference-based model for each mouse. Still, the difference was not statistically significant as an aggregate due to the large variation of R across mice.

Table 3 shows the p-values of the difference between the estimated parameters in the positive-ROI and negative-ROI (PSMA+ vs. PSMA−), and between injection of free NBs, PSMA-NBs, and MBs, as assessed by the Kolmogorov–Smirnov test. It can be observed that four estimated parameters, β, β/λ, β_+/β_-, for the mLDRW-input model, and γ for the reference-based
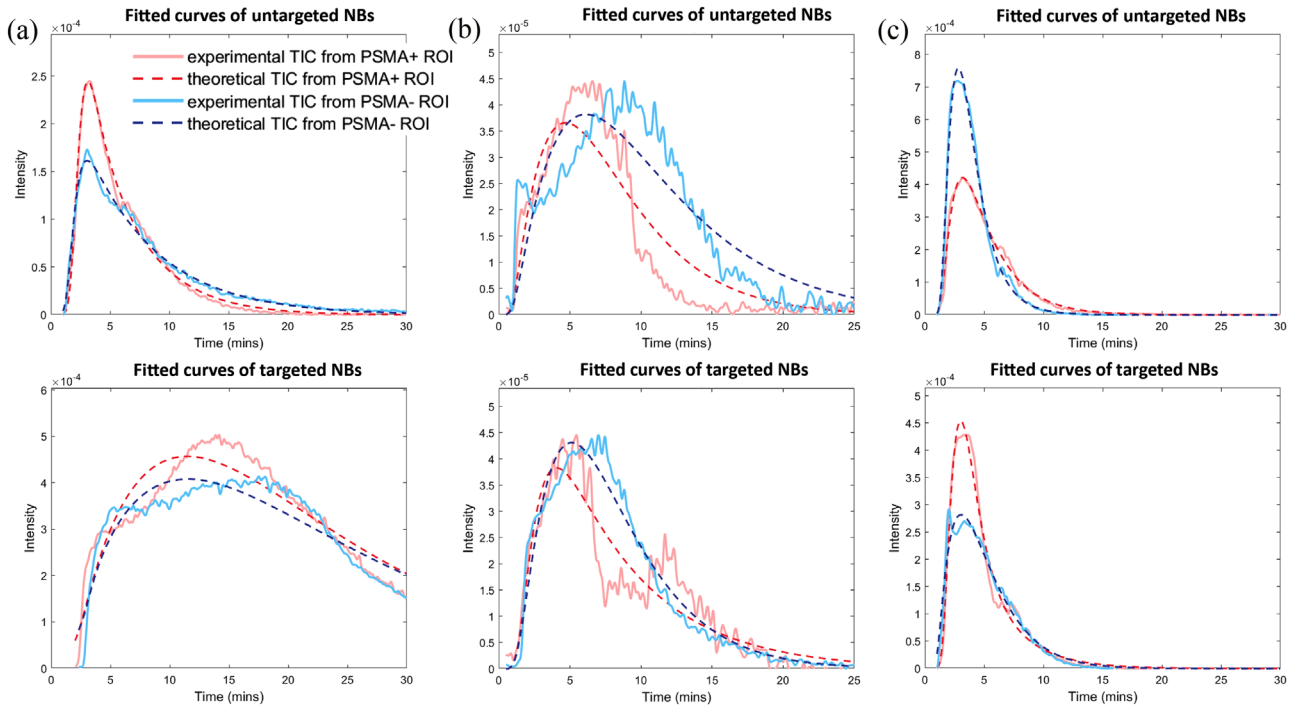
FIGURE 5 Examples of fitted curves from mouse 1 (a), mouse 5 (b), and mouse 6 (c) using the mLDRW-input model. The top and bottom rows present the TICs obtained by injection of free NBs and PSMA-NBs, respectively. Each plot consists of the experimental and fitted theoretical TICs from both PSMA-positive (PSMA+) and PSMA-negative (PSMA−) ROIs.

TABLE 2 Estimated parameters by the reference-based model

	Free NBs				PSMA-NBs				MBs			
	R_r	k_2	γ	R	R_r	k_2	γ	R	R_r	k_2	γ	R
Mouse 1	1.366	0.151	−0.036	0.14	1.040	0.344	0.096	0.11	0.626	0.601	−0.252	0.03
Mouse 2	0.979	0.371	−0.073	0.20	2.478	1.376	2.441	0.08	0.715	0.023	1.229	0.02
Mouse 3	0.345	0.237	−0.934	0.57	0.473	1.020	0.347	0.12	1.375	0.727	−0.094	0.06
Mouse 4	0.195	0.033	−0.669	0.11	0.599	0.081	0.075	0.11	0.505	0.528	−0.342	0.01
Mouse 5	2.650	0.370	−0.076	0.41	1.311	0.447	0.118	0.37	2.674	0.324	0.853	0.03
Mouse 6	0.410	0.201	−0.378	0.07	1.042	0.067	0.115	0.24	0.675	0.019	0.611	0.04
Mouse 7	1.078	0.455	−0.101	0.14	1.672	0.612	0.287	0.06	0.635	0.560	−0.302	0.02

Note: The estimated parameters input delivering ratio R_r, rate constant k_2, and binding potential γ, along with the normalized error R, are listed for seven mice, with free NBs, PSMA-NBs, and MBs presented in three major columns.

Abbreviations: NB, nanobubble; PSMA, prostate-specific membrane antigen; PSMA-NB, PSMA-targeted NB.

model, were significantly different (p-value <0.05) between free NBs and PSMA-NBs. The p-values were especially low for β_+/β_- and γ. No significant difference was noted in the comparison between PSMA-negative ROI and PSMA-positive ROI.

4 | DISCUSSION

Due to the limitations of available imaging modalities, PCa diagnosis still requires systematic biopsies, where patient discomfort, costs, and risks of hemorrhages and infections are serious drawbacks. Moreover, accurate

assessment is somehow hampered by the limited spatial sampling, resulting in over- and under-treatment of patients. Several imaging modalities have been developed to improve the detection and localization of PCa. Although multiparametric MRI is now recommended to improve the detection rate, the high cost, time-consuming workflow, and complex interpretation of the images limit its wide application outside major medical centers. As an alternative imaging modality, CEUS is a promising diagnostic tool for PCa detection with advantages, such as low cost, portability, flexibility, and minimal disruptions in the established diagnostic workflow for PCa. Conventional CEUS typically utilizes
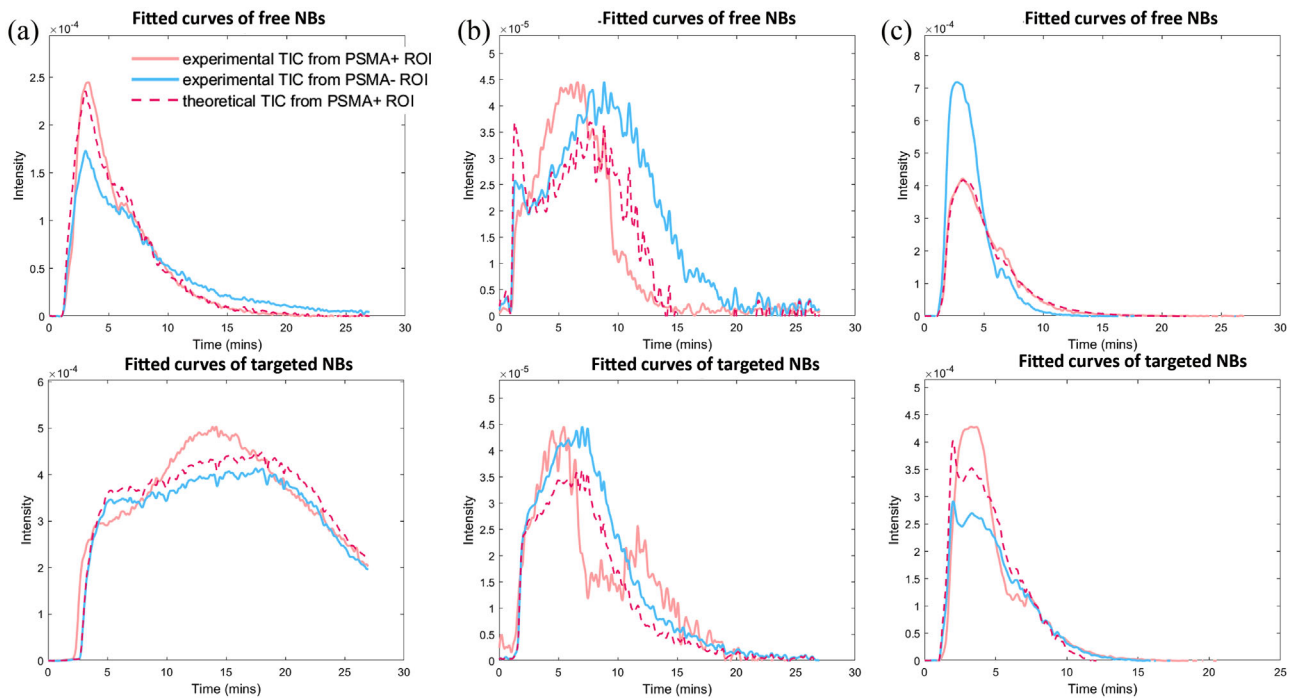
FIGURE 6 Examples of fitted curves from mouse 1 (a), mouse 5 (b), and mouse 6 (c) using the reference-based model. The top and bottom rows present the TICs obtained by injection of free NBs and PSMA-NBs, respectively. Each plot consists of the experimental TICs from PSMA-positive (PSMA+) and PSMA-negative (PSMA−) ROIs and the fitted theoretical TIC from the PSMA-positive ROI.

TABLE 3 The p-values estimated by the Kolmogorov–Smirnov test

	β	λ	κ	β/λ	β_+/β_-	k_2	γ
PSMA+ vs. PSMA−	0.423	0.883	0.423	0.423	————	————	————
PSMA-NB vs. free NBs	**0.0275**	0.129	0.129	**0.0275**	**4.42e-03**	0.423	**4.49e-04**

Note: Seven estimated parameters from the two models are compared. The upper row lists the p-values in comparing PSMA-positive (PSMA+) and PSMA-negative (PSMA−) ROIs when using PSMA-NBs. The lower row lists the p-values in the comparison between PSMA-NB and free NBs. Because β_+/β_-, k_2, and γ were estimated jointly from two ROIs (PSMA-positive and PSMA-negative ROIs), they were only compared between PSMA-targeted and free NBs.
Abbreviations: NB, nanobubble; PSMA, prostate-specific membrane antigen; PSMA-NB, PSMA-targeted NB; ROI, region of interest.

intravascular MBs to visualize their flow in the microcirculation and potentially assess angiogenic changes due to PCa development. The introduction of MBs targeted to angiogenesis has provided additional possibilities for detecting PCa. As a novel type of UCA, NBs have been proven to extravasate and access tissue targets outside of vessels. The possibility to target molecules such as PSMA, which is commonly overexpressed in PCa, opens up new avenues for functional molecular imaging using CEUS. The specific binding of PSMA-NBs was demonstrated by the prolonged retention effect in PSMA-positive PC3pip tumor in dual-tumor mouse models.[27] Our recent work also performed histological analysis of NB- and PSMA-NB-injected tumors for examining the in vivo distributions of NBs and PSMA-NBs. The confocal imaging clearly demonstrated the PSMA-NB accumulation in the tumor and additionally, the NB distribution beyond the vasculature. Going beyond qualitative or semi-quantitative analysis,

our work introduces two pharmacokinetic methods for quantitative analysis of the prolonged retention effect caused by extravasation and PSMA-specific binding.

Pharmacokinetic modeling of contrast agent intravascular flow, extravasation, and specific binding has been studied separately in MB-based CEUS, DCE-MRI, and nuclear imaging, respectively[29–32]; however, to the best of our knowledge, previous pharmacokinetic studies have never addressed extravasation with UCA in the unique size range of NBs. Thus, we adapted previous methods to be able to describe and interpret the behavior of PSMA-NBs in a dual-tumor mouse model. Most previous studies represented a biological system by compartmental modeling with an input function. Here, we developed two pharmacokinetic compartmental models of PSMA-NBs in the dual-tumor mouse model, with the input function directly or indirectly approximated. The first model is based on the description of the arterial input function as an mLDRW model, which has shown

to reasonably describe the UCA dispersion across the microvasculature in PCa.[15,37] This model needs no additional measurement on reference tissue, but the cost is a higher risk of overfitting given the increased number of parameters. The second model, based on the simplified reference-tissue model,[30] utilizes the TIC from the PSMA-negative ROI as the input to depict the TIC from the PSMA-positive ROI. This simplified model allows for quantifying specific PSMA-targeted binding without requiring an approximation of the vascular input. Compared to the mLDRW-input model, this simplified model has limited flexibility and always needs an additional tissue ROI as reference. Unlike the original definition in,[30] which restrains the binding potential to positive values, we allow this parameter to be negative to account for the possible reduced retention effect in the PSMA-positive ROI, particularly in the case of free NBs.

Regarding the curve fitting performance, the mLDRW-input model produces high fitting quality for the PSMA-positive ROI compared to the PSMA-negative ROI in each mouse, using PSMA-NBs. The lower fitting quality obtained in PSMA-positive ROIs for PSMA-NBs results from extra kinetic complexity due to specific binding. The current model, which combines the effects of extravasation and binding in one exponentially decaying function, cannot fully describe this complexity. In each mouse, the reference-based model shows an overall lower fitting quality than the mLDRW-input model. This difference can be explained by the lower flexibility provided by a smaller number of free parameters. In both models, the relatively inaccurate TIC fitting in mice 1, 3, and 5 suggests the oversimplification in modeling the specific binding merely via a separate compartment.

The primary purpose of targeting NBs to PSMA is to improve the detection of PCa through specific molecular binding. The specific binding is demonstrated by the prolonged retention period in the TICs obtained with PSMA-NBs compared to the TICs obtained with free NBs. The mLDRW-input model independently interprets the TICs from either PSMA-positive or PSMA-negative ROIs. As shown in Table 1 and Figure 4a–c, the estimated residual factor β, whose function is to scale the extravasation component of the model, is mostly higher in the PSMA-positive ROI than the PSMA-negative ROI, when using PSMA-NBs. The higher residual factor β indicates that a larger portion of PSMA-NBs is retained after the wash-in phase. Moreover, the significantly low β for MBs suggests that the prolonged retention effect of MBs is not prominent. The decay rate λ, which represents the decaying trend of overall contrast enhancement, does not exhibit a significant difference. In addition, we proposed the combined parameter β/λ to represent the relative contribution of the extravasation component to the overall AUC. As shown in Figure 4d, the parameter β/λ exhibits a similar difference as β (with the same exceptional case of mouse 6).

Different from the mLDRW-input model, the reference-based model describes the binding kinetics of an indicator in the target tissue (e.g., PSMA-positive ROI) by using a reference tissue, that is, a tissue that behaves kinetically equivalently to the target tissue, but where binding does not occur (e.g., PSMA-negative ROI). As a result, no comparison was possible between the two ROIs. As shown in Table 2 and Figure 4f,g, the estimated binding potential γ is noticeably overall positive for PSMA-NBs and overall negative for free NBs. This clear difference suggests a substantial difference in the kinetics of PSMA-NBs between PSMA-positive and PSMA-negative ROIs. It should be noted that further investigation is required to explain the reason for the all-negative γ values with free NBs. Overall, the estimated parameters β, β/λ, and γ suggest that a larger portion of PSMA-NBs is retained after the wash-in phase within the PSMA-positive ROI.

The differences in the estimated parameters were statistically assessed by the Kolmogorov–Smirnov test, which does not assume any specific probability distribution of tested samples. As listed in Table 3, our results show several parameters from both models, providing significant differences between free and PSMA-NBs. The difference between free NBs and PSMA-NBs is more significant for the parameters jointly estimated from two ROIs via the reference-based method. However, the application of the mLDRW-input model is more practical, because it does not require the presence of a reference ROI in the field of view, allowing for pixel-based TIC analysis. In general, the proposed models are both limited in terms of fitting quality and the trade-off between overfitting and flexibility. The complex TIC profiles manifested in mice 1 and 5 suggest some TIC curve features to be not fully captured by the proposed compartmental models. However, increasing the model complexity may lead to overfitting or suboptimal parameter estimation due to the larger number of fitting parameters. In the design of the animal experiments, the variation of PSMA-NB kinetics is assumed to be mainly caused by the different PSMA expressions between the two tumors. However, in practice, other factors, such as tumor characteristics and physiological conditions of the mice, will introduce other variations to the NB kinetics. Tumor heterogeneity may also affect our estimations, as the portion of the tumor visualized in the acquired imaging plane may differ from the other tumor areas. Moreover, three-dimensional ultrasound could enable a more complete characterization of the investigated tumor tissues. Because the aforementioned complex factors can prominently affect the NB and PSMA-NB kinetics shown in CEUS, the prolonged retention effect due to extravasation and specific binding is difficult to be reliably identified by qualitative or semi-quantitative analysis. The application of dedicated pharmacokinetic modeling can estimate parameters, for example, the binding potential γ and residual factor β, for

automatically and reproducibly identifying the prolonged retention effect. When PSMA-NB CEUS is adopted in future clinical practice, these estimated parameters can possibly serve as useful features in diagnosing PCa. In the future, dedicated pharmacokinetic modeling can be developed to analyze the pharmacokinetics of PSMA-NBs at the pixel level. Additionally, experiments with a larger number of samples and naturally induced tumors are expected to further validate the applicability of PSMA-NBs in detecting PCa. Moreover, immunohistological analysis of the tumor tissue should also be performed to further validate the proposed pharmacokinetic models.

5 | CONCLUSION

Quantification of NB pharmacokinetics by dedicated models evidences different behaviors between PSMA-targeted and free NBs when investigated in PSMA-positive and PSMA-negative tumors. These promising results encourage further investigations into quantitative analysis methods to describe the kinetics of targeted NBs, aiding our understanding of their transport and interaction with tissue and possibly leading to improved cancer diagnostics and characterization.

CONFLICT OF INTEREST
The authors declare they have no conflicts of interest.

REFERENCES
1. Bray F, Ferlay J, Soerjomataram I, Siegel RL, Torre LA, Jemal A. Global cancer statistics 2018: GLOBOCAN estimates of incidence and mortality worldwide for 36 cancers in 185 countries. *CA Cancer J Clin*. 2018;68:394-424.
2. Siegel RL, Miller KD, Jemal A. Cancer statistics, 2019. *CA Cancer J Clin*. 2019; 69: 7-34.
3. Taitt HE. Global trends and prostate cancer: a review of incidence, detection, and mortality as influenced by race, ethnicity, and geographic location. *Am J Mens Health*. 2018;12:1807-1823.
4. Mottet N, Bellmunt J, Bolla M, et al. EAU-ESTRO-SIOG guidelines on prostate cancer. Part 1: screening, diagnosis, and local treatment with curative intent. *Eur Urol*. 2017;71:618-629.
5. Cuzick J, Thorat MA, Andriole G, et al. Prevention and early detection of prostate cancer. *Lancet Oncol*. 2014;15:e484-e492.
6. Gosselaar C, Roobol MJ, Roemeling S, et al. The role of the digital rectal examination in subsequent screening visits in the European Randomized Study of Screening for Prostate Cancer (ERSPC), Rotterdam. *Eur Urol*. 2008;54:581-588.
7. Heidenreich A, Bastian PJ, Bellmunt J, et al. 2014 EAU guidelines on prostate cancer. Part 1: screening, diagnosis, and local treatment with curative intent–update. *Eur Urol*. 2013;65: 124-137.
8. Drost FJH, Osses D, Nieboer D, et al. Prostate magnetic resonance imaging, with or without magnetic resonance imaging-targeted biopsy, and systematic biopsy for detecting prostate cancer: a Cochrane systematic review and meta-analysis. *Eur Urol*. 2020;77:78-94.
9. Kasivisvanathan V, Rannikko AS, Borghi M, et al. MRI-targeted or standard biopsy for prostate-cancer diagnosis. *N Engl J Med*. 2018;378:1767-1777.
10. Pallwein L, Mitterberger M, Pelzer A, et al. Ultrasound of prostate cancer: recent advances. *Eur Radiol*. 2008;18:707-715.
11. Drudi FM, Cantisani V, Angelini F, et al. Multiparametric MRI versus Multiparametric US in the detection of prostate cancer. *Anticancer Res*. 2019;39:3101-3110.
12. Halpern EJ. Contrast-enhanced ultrasound imaging of prostate cancer. *Rev Urol*. 2006;8:S29.
13. Harvey C, Pilcher J, Richenberg J, et al. Applications of transrectal ultrasound in prostate cancer. *Br J Radiol*. 2012;85:S3-S17.
14. Russo G, Mischi M, Scheepens W, et al. Angiogenesis in prostate cancer: onset, progression and imaging. *BJU Int*. 2012;110:E794-E808.
15. Kuenen MP, Mischi M, Wijkstra H. Contrast-ultrasound diffusion imaging for localization of prostate cancer. *IEEE Trans Med Imaging*. 2011;30:1493-1502.
16. Van Sloun RJ, Demi L, Postema AW, et al. Ultrasound-contrast-agent dispersion and velocity imaging for prostate cancer localization. *Med Image Anal*. 2017;35:610-619.
17. Smeenge M, Tranquart F, Mannaerts CK, et al. First-in-human ultrasound molecular imaging with a VEGFR2-specific ultrasound molecular contrast agent (BR55) in prostate cancer: a safety and feasibility pilot study. *Invest Radiol*. 2017;52: 419-427.
18. Wu H, Abenojar EC, Perera R, An T, et al. Time-intensity-curve analysis and tumor extravasation of nanobubble ultrasound contrast agents. *Ultrasound Med Biol*. 2019;45:2502-2514.
19. Perera RH, Hernandez C, Zhou H, et al. Ultrasound imaging beyond the vasculature with new generation contrast agents. *Wiley Interdiscip Rev Nanomed Nanobiotechnol*. 2015;7:593-608.
20. Perera RH, Wu H, Peiris P, et al. Improving performance of nanoscale ultrasound contrast agents using N-diethylacrylamide stabilization. *Nanomedicine*. 2017;13:59-67.
21. Perera R, Hernandez C, Cooley M, et al. Contrast enhanced ultrasound imaging by nature-inspired ultrastable echogenic nanobubbles. *Nanoscale*. 2019;11:15647-15658.
22. Wu H, Rognin NG, Krupka TM, et al. Acoustic characterization and pharmacokinetic analyses of new nanobubble ultrasound contrast agents. *Ultrasound Med Biol*. 2013;39: 2137-2146.
23. Ramirez DG, Abenojar E, Hernandez C, et al. Contrast-enhanced ultrasound with sub-micron sized contrast agents detects insulitis in mouse models of type1 diabetes. *Nat Commun*. 2020;11: 2238.
24. Gao Y, Hernandez C, Yuan HX, et al. Ultrasound molecular imaging of ovarian cancer with CA-125 targeted nanobubble contrast agents. *Nanomedicine*. 2017;13:2159-2168.
25. Perera R, Wang X, Ramamurtri G, et al. IEEE International Ultrasonics Symposium (IUS). 2018:1-4. https://doi.org/10.1109/ULTSYM.2018.8580221
26. Han S, Woo S, Kim Y, et al. Impact of 68Ga-PSMA PET on the management of patients with prostate cancer: a systematic review and meta-analysis. *Eur Urol*. 2018;74:179-190.
27. Perera RH, Wang X, Wang Y, et al. Real time ultrasound molecular imaging of prostate cancer with PSMA-targeted nanobubbles. *Nanomedicine*. 2020;28:102213.

28. Wang Y, Perera R, Abenojar E, et al. Molecular imaging of orthotopic prostate cancer with nanobubble ultrasound contrast agents targeted to PSMA. *Sci Rep*. 2021;11:4726.

29. Turco S, Tardy I, Frinking P, et al. Quantitative ultrasound molecular imaging by modeling the binding kinetics of targeted contrast agent. *Phys Med Biol*. 2017;62:2449.

30. Lammertsma AA, Hume SP. Simplified reference tissue model for PET receptor studies. *Neuroimage*. 1996;4:153-158.

31. Lammertsma A, Bench C, Hume S, et al. Comparison of methods for analysis of clinical [11C]raclopride studies. *J Cereb Blood Flow Metab*. 1996;16:42-52.

32. Mischi M, Turco S, Lavini C, et al. Magnetic resonance dispersion imaging for localization of angiogenesis and cancer growth. *Invest Radiol*. 2014;49:561-569.

33. Cobelli C, Carson E. *Introduction to Modeling in Physiology and Medicine*. Academic Press; 2019.

34. Jacquez JA, Simon CP. Qualitative theory of compartmental systems. *SIAM Rev*. 1993;35:43-79.

35. Turco S, Perera RH, Wijkstra H. IEEE International Ultrasonics Symposium (IUS). 2019:399-402. https://doi.org/10.1109/ULTSYM.2019.8925563

36. Perera R, Abenojar E, Nittayacharn P, et al. 2021 intracellular vesicle entrapment of nanobubble ultrasound contrast agents targeted to PSMA promotes prolonged enhancement and stability in vivo and in vitro. *Nanotheranostics*. 2022;6:270-285.

37. Turco S, Wijkstra H, Mischi M. Mathematical models of contrast transport kinetics for cancer diagnostic imaging: a review. *IEEE Rev Biomed Eng*. 2016;9:121-147.

SUPPORTING INFORMATION

Additional supporting information can be found online in the Supporting Information section at the end of this article.